



**HAL**  
open science

# Spectroscopic study of nitrogen incorporation in Ge, Sb, and Te elemental systems: A step toward the understanding of nitrogen effect in phase-change materials

L Prazakova, E Nolot, Eugénie Martinez, D Rouchon, N Rochat, C Sabbione, J Li, D Eichert, G Pepponi, M Bernard, et al.

## ► To cite this version:

L Prazakova, E Nolot, Eugénie Martinez, D Rouchon, N Rochat, et al.. Spectroscopic study of nitrogen incorporation in Ge, Sb, and Te elemental systems: A step toward the understanding of nitrogen effect in phase-change materials. *Journal of Applied Physics*, 2022, 132, pp.205102. 10.1063/5.0117596 . cea-04565947

**HAL Id: cea-04565947**

**<https://cea.hal.science/cea-04565947>**

Submitted on 2 May 2024

**HAL** is a multi-disciplinary open access archive for the deposit and dissemination of scientific research documents, whether they are published or not. The documents may come from teaching and research institutions in France or abroad, or from public or private research centers.

L'archive ouverte pluridisciplinaire **HAL**, est destinée au dépôt et à la diffusion de documents scientifiques de niveau recherche, publiés ou non, émanant des établissements d'enseignement et de recherche français ou étrangers, des laboratoires publics ou privés.

# Spectroscopic study of nitrogen incorporation in Ge, Sb, and Te elemental systems: A step toward the understanding of nitrogen effect in phase-change materials

Cite as: J. Appl. Phys. **132**, 205102 (2022); <https://doi.org/10.1063/5.0117596>

Submitted: 23 August 2022 • Accepted: 31 October 2022 • Published Online: 22 November 2022

 L. Prazakova,  E. Nolot, E. Martinez, et al.



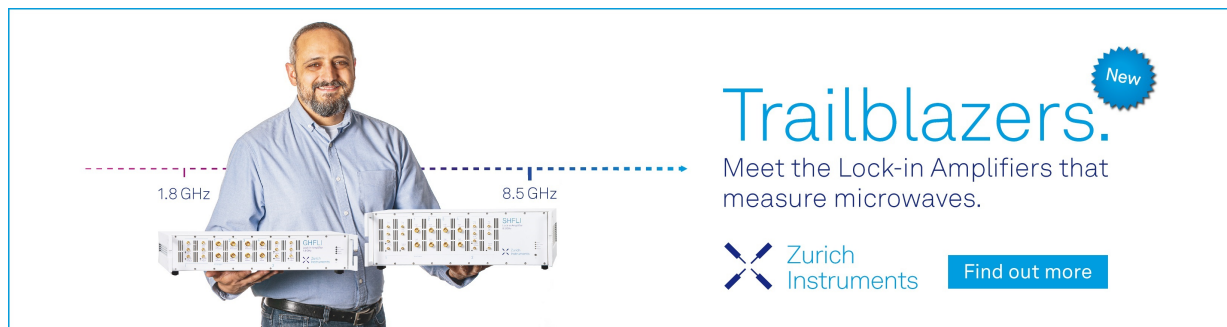
View Online




Export Citation




CrossMark



**Trailblazers.** 

Meet the Lock-in Amplifiers that measure microwaves.

 Zurich Instruments [Find out more](#)

# Spectroscopic study of nitrogen incorporation in Ge, Sb, and Te elemental systems: A step toward the understanding of nitrogen effect in phase-change materials

Cite as: J. Appl. Phys. **132**, 205102 (2022); doi: [10.1063/5.0117596](https://doi.org/10.1063/5.0117596)

Submitted: 23 August 2022 · Accepted: 31 October 2022 ·

Published Online: 22 November 2022



View Online



Export Citation



CrossMark

L. Prazakova,<sup>1</sup> E. Nolot,<sup>1,a)</sup> E. Martinez,<sup>1</sup> D. Rouchon,<sup>1</sup> N. Rochat,<sup>1</sup> C. Sabbione,<sup>1</sup> J. Li,<sup>1</sup> D. Eichert,<sup>2</sup> G. Pepponi,<sup>3</sup> M. Bernard,<sup>1</sup> and G. Navarro<sup>1,a)</sup>

## AFFILIATIONS

<sup>1</sup>Univ. Grenoble Alpes, CEA, Leti, F-38000, Grenoble, France

<sup>2</sup>Elettra Sincrotrone Trieste S.C.p.A, Trieste 34149, Italy

<sup>3</sup>FBK—CMM—Micro Nano Facility 38123, Trento, Italy

<sup>a)</sup>Authors to whom correspondence should be addressed: [emmanuel.nolot@cea.fr](mailto:emmanuel.nolot@cea.fr) and [gabriele.navarro@cea.fr](mailto:gabriele.navarro@cea.fr)

## ABSTRACT

Nitrogen doping in chalcogenide materials represents a promising way for the improvement of material properties. Indeed, N doping in GeSbTe phase-change alloys have demonstrated to greatly enhance thermal stability of their amorphous phase, necessary to ensure the data retention of the final phase-change memory device. Although it is suggested that the N doping in such alloys leads to the preferential formation of Ge-N bonds, further questions concerning the bonding, in particular, Sb-N and Te-N, and the structural arrangement remain unclear. In this paper, we present a study of as-deposited elemental Ge, Sb, and Te systems and their nitrides (i.e., GeN, SbN, and TeN alloys), using a large range of N content from 0 up to about 50 at. %. The as-deposited alloys are investigated by Fourier transform infrared and Raman spectroscopy. We identify the active vibrational modes associated with the formation of Ge-N, Sb-N, and Te-N bonds, highlighting the impact of N incorporation on the structure of these elemental systems. We further qualitatively compare the GeN, SbN, and TeN experimental spectra with the “*ab initio*” simulations of the related ideal nitride structures. Finally, the analysis of elemental nitride layers is extended to N-doped GeSbTe alloys, providing deeper understanding of nitrogen bonding in such ternary systems, employed in memory technology.

Published under an exclusive license by AIP Publishing. <https://doi.org/10.1063/5.0117596>

## I. INTRODUCTION

Germanium, antimony, and tellurium are metalloids considered as “technology critical elements.”<sup>1,2</sup> Either pure or alloyed in more complex systems, these elements are used for a wide range of applications in optics, photonics, microelectronics, and solar cells industry.<sup>3–10</sup> The binary (GeTe, SbTe) and ternary (GeSbTe) chalcogenide alloys are widely investigated in the field of phase-change memory (PCM) technology for their phase-change properties, based on the reversible transition between their amorphous and crystalline phases.<sup>11–14</sup> Indeed, ternary GeSbTe alloys have already proven their maturity in the memory device industry.<sup>15–18</sup> Material engineering of GeSbTe alloys (GST) have been extensively investigated over the past

years as a possible approach to improve the phase-change material properties. The two most common approaches have been: (a) the stoichiometry tuning<sup>19–22</sup> and the exploration of off-stoichiometric alloys (i.e., Ge-rich or Sb-rich alloys); (b) the doping of the alloy by other elements, such as C, N, O, or Si.<sup>23–29</sup> The benefit of N doping in chalcogenide materials to improve the phase-change properties is known since their use in optical applications.<sup>12,30</sup> It has been suggested that N doping in these alloys leads to the formation of Ge-N bonds, which are responsible for the increase of crystallization temperature and the reduction of the grain size of the formed GST crystalline phase.<sup>31–33</sup> However, the effect of N incorporation in GeSbTe alloys raised several questions concerning the bonding configuration

and the related structural arrangement. In particular, the possible bond formation implying Sb and Te is still under debate.

Germanium nitride (GeN) alloys were systematically studied in the past, owing to the great interest in Ge as a material for microelectronics and to its structural similarities with conventional Si.<sup>34–39</sup> Ge<sub>3</sub>N<sub>4</sub> is considered as a stable stoichiometric compound. In contrast, antimony nitrides (SbN) and tellurium nitrides (TeN) have been less studied so far and their structure is rather unknown. GeN, SbN, TeN, and their N-doped binary and ternary alloys were investigated by X-ray photoelectron spectroscopy (XPS)<sup>40</sup> and a map of inorganic nitrides was suggested in Ref. 41, predicting the formation of binary nitrides and calculating their formation enthalpies. While the formation enthalpy of the GeN system is about -0.25 eV/at (Ge<sub>3</sub>N<sub>4</sub> structure), the calculated value for SbN system increases to 0.18 eV/at (SbN structure) and for the TeN system to 0.68 eV/at (Te<sub>3</sub>N<sub>4</sub> structure; 1.09 eV/at for the TeN<sub>2</sub> structure).<sup>41,42</sup> These values indicate the high stability of the GeN system, while the formation of SbN and TeN is much less favorable. Indeed, the formation of Te<sub>3</sub>N<sub>4</sub> is suggested but the structure is considered highly unstable,<sup>43,44</sup> while some studies report about SbN formation and stability only at high pressures.<sup>45,46</sup>

In this work, we present the investigation of as-deposited Ge, Sb, and Te thin layers upon the nitrogen incorporation, studied by Raman and FTIR spectroscopy. We reveal the impact of nitrogen on the structure of Ge, Sb, and Te, and we identify the vibrational bands in the spectra related to the Ge-N, Sb-N, and Te-N bonds. The experimental IR and Raman results are supported by X-ray absorption spectroscopy (XAS) measurements performed on the as-deposited layers and by “*ab initio*” simulations of the related ideal nitride structures. Finally, we analyze the spectra of N-doped ternary GeSbTe alloys (N content lower than 10 at. %) in the light of the results obtained from elemental nitride layers, underlining the main effects of nitrogen incorporation in ternary alloys, recently considered for memory applications.

## II. EXPERIMENTAL METHODS

Elemental Ge, Sb, and Te layers were deposited on 200 mm Si (100) wafers by magnetron sputtering from Ge, Sb, and Te targets, respectively, in Ar atmosphere. The nitride layers (i.e., GeN, SbN, and TeN) were prepared by reactive sputtering in an Ar/N<sub>2</sub> gas mixture in the deposition chamber. GeN, SbN, and TeN layers with different N contents resulted from the variation of the ratio between Ar and N<sub>2</sub> gas flows during film deposition. The N<sub>2</sub> flow was varied from 0.5 SCCM up to 40 SCCM. In the following, we will address the nitride layers referring to the used N<sub>2</sub> flow. The deposition of all layers was performed at room temperature and the as-deposited 100 nm-thick layers were protected by a 3.5 nm-thick carbon capping layer deposited *in situ* without air exposure to prevent surface oxidation.

The composition of the layers was measured by wavelength dispersive X-ray fluorescence spectroscopy (WDXRF Rigaku AZX 400) using the methodology described in Ref. 47. The IR transmittance spectra converted to absorbance were acquired in the range from 4000 to 30 cm<sup>-1</sup> (Bruker Vertex 70VA) with the resolution of 4 cm<sup>-1</sup>, accumulating 64 scans. The IR spectra in the range below 1000 cm<sup>-1</sup> are presented as no bands are observed at higher

wavenumbers (except the TeN 20 SCCM layer, specified later in the text). The Raman spectroscopy measurements (Renishaw InVia) were performed in the Raman shift range from 100 to 1000 cm<sup>-1</sup>, using the 532 nm laser excitation source and the focusing lens with the magnitude 100× and numerical aperture 0.85. The applied laser power was kept below 0.6 mW.

The local atomic structure has been studied by extended X-ray absorption fine structure (EXAFS) and X-ray near-edge spectroscopy (XANES) techniques at the XRF beamline at Elettra Sincrotrone Trieste, Italy. The Ge-K EXAFS measurement, Sb-L<sub>3</sub>, and Te-L<sub>3</sub> XANES measurements were performed in a fluorescence mode for elemental (Ge, Sb, and Te) and nitride (GeN, SbN, and TeN) samples, respectively. Theoretical EXAFS functions for Ge-Ge and Ge-N pairs were generated using the FEFF program package.<sup>48</sup>

The “*ab initio*” simulations of IR and Raman spectra were performed on Ge, Sb, and Te nitride structures in order to identify the active vibrational modes assigned to N bonding with Ge, Sb, or Te in the respective ideal crystalline structures. The identification of IR- and Raman-active modes of the related nitride structures allows to determine possible N bonding contributions in the studied amorphous layers. The simulations were performed using VASP code<sup>49,50</sup> and Phonopy-Spectroscopy package.<sup>51</sup> Initial crystal structures of Ge<sub>3</sub>N<sub>4</sub>, SbN, and TeN<sub>2</sub> were obtained from Materials Project,<sup>42</sup> followed by structural relaxation using density functional theory (DFT) with a Monkhorst-Pack (MP) mesh (4 × 8 × 8 for Ge<sub>3</sub>N<sub>4</sub> and 6 × 6 × 6 for SbN and TeN<sub>2</sub>). Phonon modes were obtained using density functional perturbation theory with a 2 × 2 × 4 supercell and a 2 × 2 × 2 MP mesh for Ge<sub>3</sub>N<sub>4</sub>; a 3 × 3 × 2 supercell and a 2 × 2 × 3 MP mesh for SbN; a 2 × 2 × 3 supercell and a 3 × 3 × 2 MP mesh for TeN<sub>2</sub>. The projector augmented wave (PAW) method with the PBE functional<sup>52</sup> and 400 eV cut-off energy were used for the calculations. For the qualitative comparison of simulated and experimental data, the obtained spectra were normalized with respect to the most intense peak of the spectra.

## III. RESULTS AND DISCUSSION

We start by presenting the quantification of the nitrogen content measured by WDXRF. Next, we present the results along with the discussion for Ge, Sb, and Te systems upon the N incorporation. Finally, we compare the results of elemental nitride layers with N-doped Ge-rich and Sb-rich GeSbTe alloys to highlight the formation of N bonding in these ternary alloys.

### A. Quantification of N content

The quantification of N content in the studied layers by the WDXRF measurements is presented in Fig. 1. The Ge and Sb layers feature the highest N incorporation with regard to the N<sub>2</sub> flow during the deposition. On the contrary, Te layers showed to be the least prone to incorporate N. The values of measured N content in the layers prepared with the N<sub>2</sub> flow of 2, 10, and 20 SCCM are listed in Table I. The tendency of the systems to incorporate nitrogen is likely related to the possibility to form the corresponding X-N bonds (where the X=Ge, Sb, or Te), as can be predicted from formation enthalpies of known nitride structures previously reported. As already mentioned above, germanium

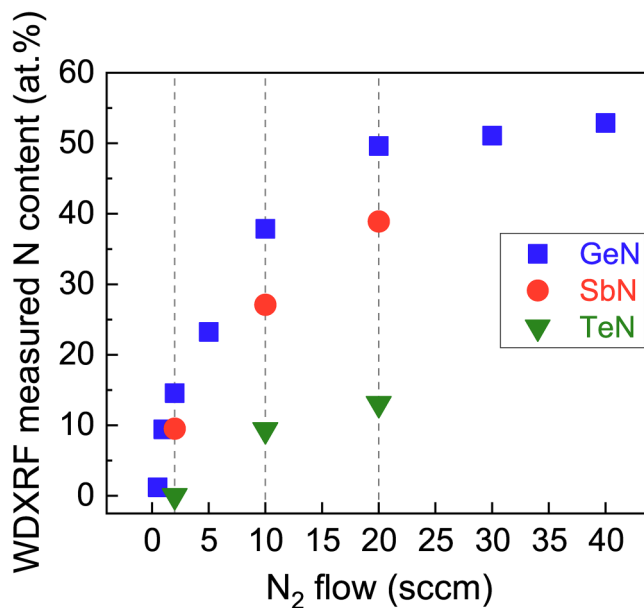


**FIG. 1.** N content in Ge, Sb, and Te nitride layers measured by WDXRF as a function of N<sub>2</sub> flow during the deposition. Dashed lines indicate the N<sub>2</sub> flow of 2, 10, and 20 SCCM. The highest incorporated N content is observed for GeN layers.

nitride presents the most stable nitride structure among the studied elemental compounds.

## B. Ge and GeN layers

IR and Raman spectra of Ge and GeN layers are shown in Fig. 2. The IR spectrum of pure Ge layer is not shown due to the lack of absorption features. Nitrogen incorporation in Ge produces a strong IR absorption band at about 690 cm<sup>-1</sup> and a second broad band at about 300 cm<sup>-1</sup>. Based on the investigation of GeN and GeN:H alloys,<sup>36,53–55</sup> these bands are related to in-plane asymmetric stretching and disorder-induced breathing vibrational modes of the Ge<sub>3</sub>N skeletal group, respectively. The asymmetric form of both bands in the IR spectra becomes more evident with increasing N content and indicates the presence of more than one contribution. Indeed, based on the performed spectra deconvolution (see the [supplementary material](#)), following contributions were identified:

**TABLE I.** Comparison of the N content in Ge, Sb and Te for the N<sub>2</sub> flow of 2, 10, and 20 SCCM.

N <sub>2</sub> flow	N content (at. %)		
	GeN	SbN	TeN
2 SCCM	14.5	9.5	0
10 SCCM	37.9	27.0	9.3
20 SCCM	49.6	38.9	13.1

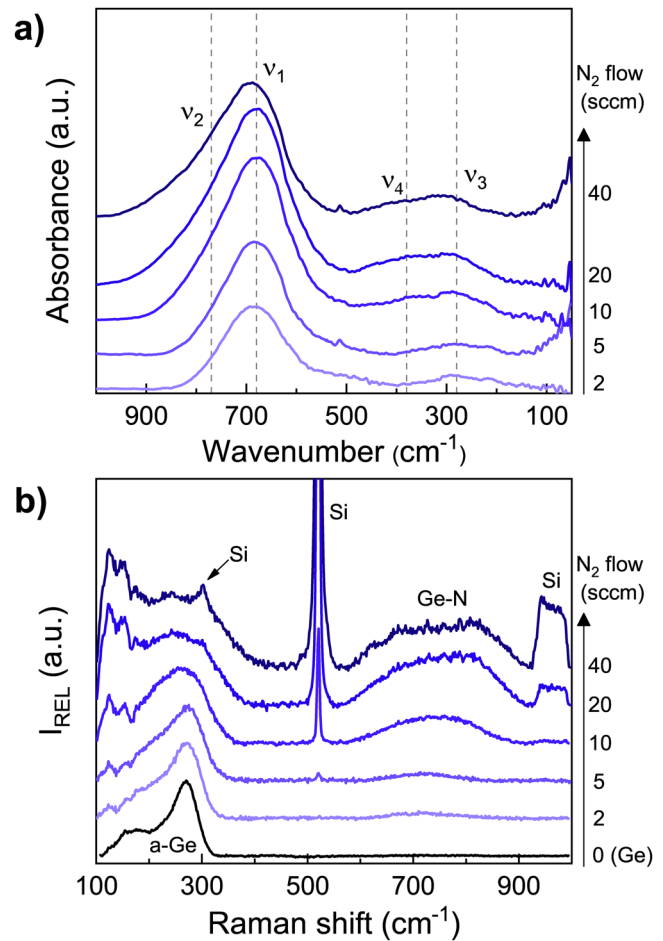


**FIG. 2.** IR (a) and Raman (b) spectra of Ge and GeN layers. IR spectra highlight the main band at about 700 cm<sup>-1</sup> and the second broad band at about 300 cm<sup>-1</sup>, each of them formed by two contributions (v<sub>1</sub> and v<sub>2</sub>; v<sub>3</sub> and v<sub>4</sub>, respectively). Raman spectra demonstrate the broadening of a-Ge modes (100–300 cm<sup>-1</sup>) and the appearance of the broad band related to vibrations of Ge-N bonds (600–800 cm<sup>-1</sup>) upon increasing N content.

main contributions at 680 cm<sup>-1</sup> (v<sub>1</sub>) and 280 cm<sup>-1</sup> (v<sub>3</sub>) accompanied by additional contributions at 750 cm<sup>-1</sup> (v<sub>2</sub>) and at 390 cm<sup>-1</sup> (v<sub>4</sub>). The integrated intensity of the GeN bands increases with N content, reaching the maximum value for GeN 20 SCCM. The same trend was observed in previous investigations.<sup>39,55</sup> However, the intensity decrease is observed in our studies for highly doped GeN compositions (i.e., N content about 50 at. %), while the band broadening still continues (Fig. 3).

Raman spectrum of Ge layer shows the characteristic band in the range from 100 to 300 cm<sup>-1</sup>. This band is assigned to amorphous Ge (a-Ge) modes, i.e., TO-like mode (275 cm<sup>-1</sup>), LO-like mode (220 cm<sup>-1</sup>), and LA-like mode (160 cm<sup>-1</sup>).<sup>39,56,57</sup> The TA-like mode is not observed in this work as it appears at wavenumbers below the edge of the used notch filter. The significant broadening of the a-Ge band is noticed upon increasing N content.

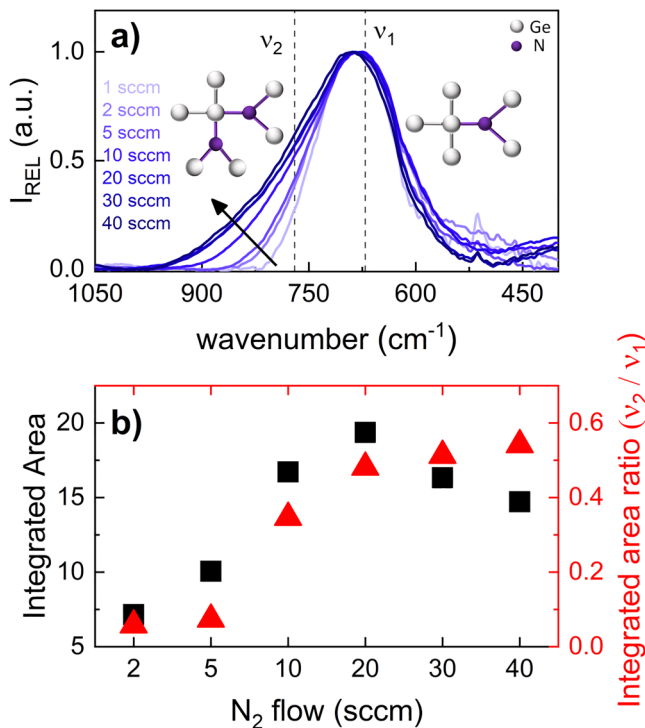


**FIG. 3.** (a) Normalized IR band, highlighting the shoulder broadening with increasing N content. The dashed lines indicate the positions of main ( $v_1$ ) and additional ( $v_2$ ) contributions. The inset sketches illustrate the bonding arrangement between Ge and N atoms. (b) Calculated values of IR band area plotted as a function of  $N_2$  flow: Integrated area of entire IR band (black squares) and the ratio of integrated areas of its contributions (area of additional contribution  $v_2$  at  $750\text{ cm}^{-1}$  over the area of the main contribution  $v_1$  at  $680\text{ cm}^{-1}$ , red triangles).

Moreover, a new broad band with the maximum at about  $700\text{ cm}^{-1}$  appears in the spectra. This band is assigned to the vibrations of the  $\text{Ge}_3\text{N}$  group, as observed in IR spectra.<sup>39</sup> More than one contribution to this band can be distinguished, in particular, in spectra of GeN with high N content (about 50 at.%, i.e., from GeN 20 SCCM), which can be correlated with the different band contributions identified in the IR spectra. The contributions of vibrational modes originating from the Si substrate also become evident in the GeN Raman spectra: the main peak at  $521\text{ cm}^{-1}$ , second order scattering modes at  $950\text{ cm}^{-1}$  and at  $300\text{ cm}^{-1}$  (in GeN 40 SCCM).<sup>58,59</sup> Their intensities increase with the N content due to progressive transparency of the GeN layers related to the changes in optical properties.<sup>39</sup>

The presence of additional contributions in the main band in IR spectra (at  $690\text{ cm}^{-1}$ ) was described in Refs. 39 and 55. The N incorporation leads to changes in the local environment, in which more Ge atoms are bonded to nitrogen. Causing the inductive effects and modifications in charge distribution around the Ge atoms, these changes result in the shift in the main vibrational energy to higher wavenumbers and to consequent appearance of an

additional contribution  $v_2$ . As the layers feature a high degree of disorder, further increasing with N incorporation, this additional contribution  $v_2$  represents the overall sum of possible different Ge-N bonds configurations. Therefore, the integrated intensity of the main IR band at about  $690\text{ cm}^{-1}$  increases with the formation of new Ge-N bonds. However, the continuous formation of Ge-N bonds leads to the saturation of the system, resulting in a maximum intensity of the IR band for GeN 20 SCCM (N content about 50 at.%). Indeed, the vibration of the  $\text{Ge}_3\text{N}$  group becomes highly affected by the large presence of neighboring Ge-N bonds, thus causing the reduction of its vibrational mode  $v_1$  at  $680\text{ cm}^{-1}$ . This results in the reduction of the band integrated intensity in the layers with higher N content, even though the broad additional contribution  $v_2$  at  $750\text{ cm}^{-1}$  continues to slightly grow (Fig. 3), leading to the preponderance of the configurations richer in N atoms.

The disorder increase in the layer upon the N incorporation and the formation of new Ge-N bonds also cause the broadening of the a-Ge modes in Raman spectra. These results are supported by the EXAFS analyses shown in Fig. 4. The Fourier transform of Ge-K EXAFS signal for the Ge layer features only one contribution corresponding to the Ge-Ge distance.<sup>37,60</sup> A second additional contribution is observed in the GeN layers at a shorter distance, corresponding to the Ge-N pair.<sup>37,60</sup> The Ge-Ge peak reduces in intensity, while the Ge-N peak increases with N incorporation. The reduction of the Ge-Ge contribution in GeN layers explains the extensive broadening (and gradual disappearance) of a-Ge modes in Raman spectra.

The analysis of IR and Raman spectra are further supported by “*ab initio*” IR and Raman simulations of active vibrational modes of crystalline hexagonal  $\text{Ge}_3\text{N}_4$ , referred as a stable germanium nitride structure.<sup>39,61</sup> The comparison between the simulated and experimental IR and Raman spectra is presented in Fig. 5. Both simulated IR and Raman spectra show good agreement with

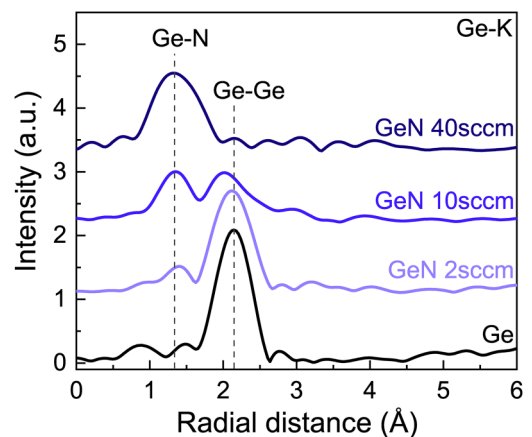


**FIG. 4.** Fourier transform (FT) of EXAFS Ge-K signal of Ge and GeN layers, demonstrating the contributions corresponding to Ge-Ge and Ge-N distances. The Ge-N contribution becomes dominant with increasing N content, at expense of the Ge-Ge contribution.



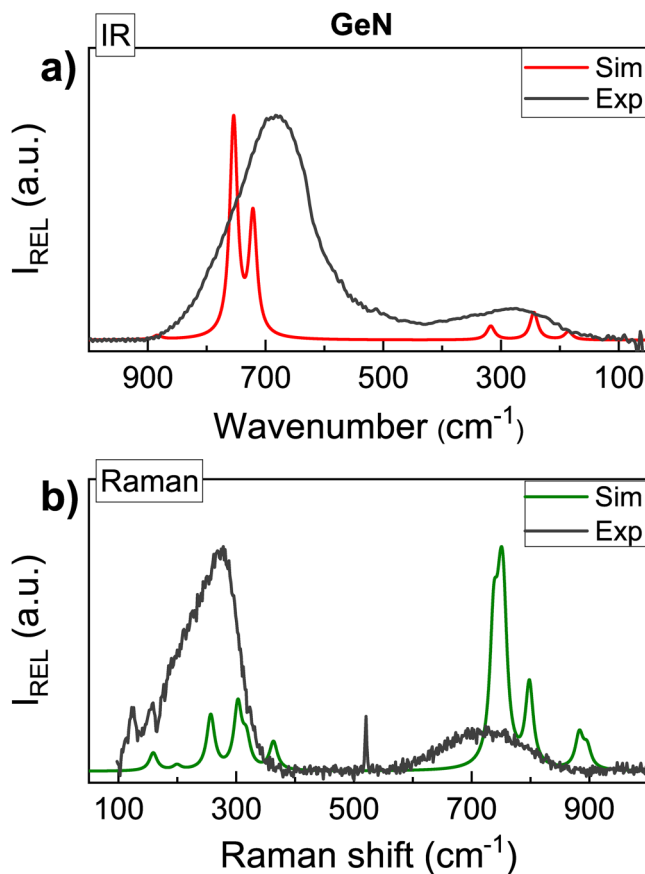


FIG. 5: Experimental (Exp) and simulated (Sim) spectra of GeN: (a) IR spectra, (b) Raman spectra. Experimental data are obtained for GeN 10 SCCM, while simulated spectra are for crystalline  $\text{Ge}_3\text{N}_4$  with hexagonal structure.<sup>42</sup>

our experimental results concerning the vibrational regions and the presence of multiple contributions in the observed regions. Moreover, the simulated Raman spectrum features several contributions at about  $300\text{ cm}^{-1}$ , which could possibly also contribute to the broadening to the band assigned to a-Ge.

### C. Sb and SbN layers

IR and Raman spectra of Sb and SbN layers are shown in Fig. 6. Antimony is known to be IR-inactive in the explored wavenumbers range (IR spectrum not shown). On the contrary, Raman spectrum of Sb layer shows two sharp peaks at  $115$  and  $150\text{ cm}^{-1}$  corresponding, respectively to  $E_g$  and  $A_{1g}$  modes of crystalline Sb.<sup>62,63</sup> A second order scattering mode at about  $270\text{ cm}^{-1}$  can be also observed.<sup>63</sup> This indicates the crystalline character of the as-deposited Sb layer. Indeed, fast spontaneous crystallization of Sb at room temperature is reported in the literature.<sup>63,64</sup>

IR spectra of SbN layers feature a broad band at  $600\text{ cm}^{-1}$ , whose intensity increases with the N content in the layer. The asymmetric form of the band suggests the presence of more than

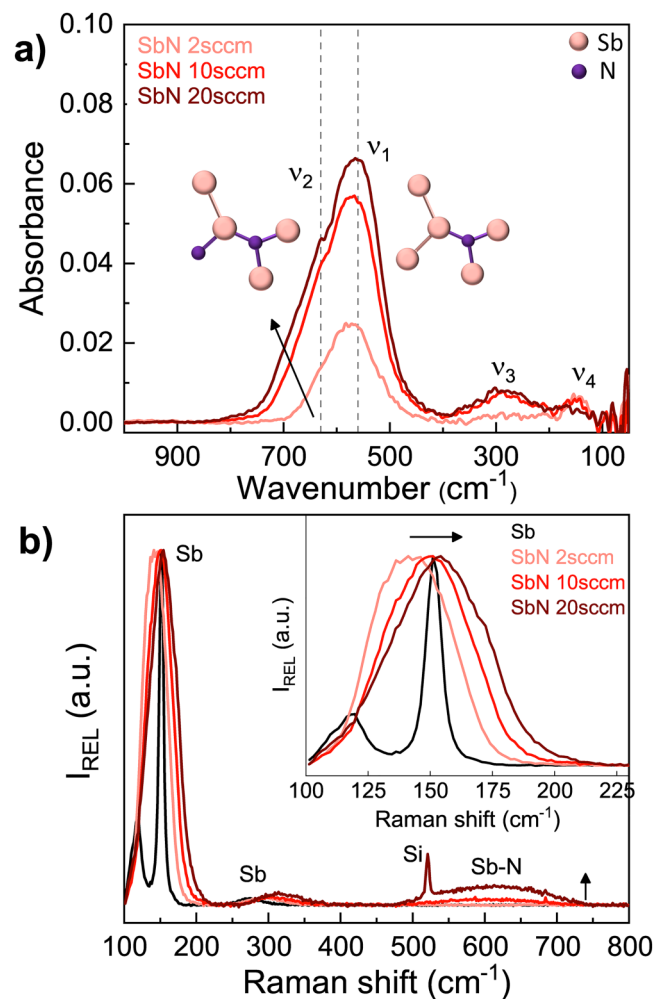


FIG. 6: IR (a) and Raman (b) spectra of Sb and SbN layers. The IR spectra show the main absorption band at about  $600\text{ cm}^{-1}$ , highlighting two possible contributions ( $v_1$  and  $v_2$ ). The inset sketches illustrate the bonding arrangement between Sb and N atoms. Raman spectra highlight two sharp peaks of crystalline Sb, broadened into one sharp band upon N incorporation. The inset in Fig. 6(b) shows a zoom of Raman spectra in the range of  $100\text{--}225\text{ cm}^{-1}$ , highlighting the band shift due to the increasing Sb-N band contribution.

one contribution. Based on the performed deconvolution (see the [supplementary material](#)), the main contribution  $v_1$  was found at  $\sim 560\text{ cm}^{-1}$  accompanied by an additional band  $v_2$  at  $\sim 630\text{ cm}^{-1}$ . Other bands are observed at about  $300\text{ cm}^{-1}$  ( $v_3$ ) and  $145\text{ cm}^{-1}$  ( $v_4$ ). The intensity of the band  $v_3$  also increases with N content, while the intensity of the band  $v_4$  is reduced. N incorporation in Sb layers results in significant changes in Raman spectra. The SbN Raman spectra of feature one broad band in the range between  $100$  and  $200\text{ cm}^{-1}$  instead of the sharp peaks observed for crystalline Sb. This may indicate the amorphous nature of the structure of Sb layers upon the N incorporation. Indeed, a similar band has been observed in the Raman spectra of undoped amorphous Sb (a-Sb).<sup>64</sup>

Furthermore, a shift of the band toward higher wavenumbers is observed with increasing N content [inset of Fig. 6(b)]. The shift is related to the increasing intensity of the band contribution at about  $170\text{ cm}^{-1}$  assigned to Sb–N bonds, as identified from spectra deconvolution (see the [supplementary material](#)). N incorporation shows to also affect the Sb second order scattering mode (at about  $270\text{ cm}^{-1}$ ), causing its broadening. Moreover, a new broad band with a maximum at  $600\text{ cm}^{-1}$  is observed in the spectra (in particular, for SbN 20 SCCM), corresponding to the wavenumber of the main band in IR spectra. The small sharp peak at  $520\text{ cm}^{-1}$  in the spectrum of SbN 20 SCCM is assigned to the Si mode of the substrate.

Crystalline Sb has a rhombohedral structure with a threefold coordination symmetry.<sup>65</sup> Sb and N elements belong to the same group of periodic table; hence they have the same valence electrons number and coordination. The same coordination of Sb and N likely facilitates the Sb atoms substitution by N atoms, leading to the formation of Sb–N bonds. This can also explain the high N incorporation into Sb layers, as shown in Fig. 1. The substitution of Sb by N atoms was already observed in N-doped GaSb alloys.<sup>66</sup> The Sb atoms substitution by N atoms and the formation of Sb–N bonds lead to the increased disorder in the layer. Indeed, nitrogen atoms have a smaller atomic radius compared to Sb, which causes the Sb atoms' displacement from their original lattice positions and thus the breaking of the long-range order in the Sb crystalline structure. This is evidenced in Raman spectra, where the Sb crystalline peaks enlarge into one broad amorphous band. The significant changes in the local atomic environment around the Sb atoms are further confirmed by XANES spectra of Sb and SbN layers, where the diminution of absorption features in the near-edge region is observed of SbN layers (Fig. 7). Similar disappearance of the

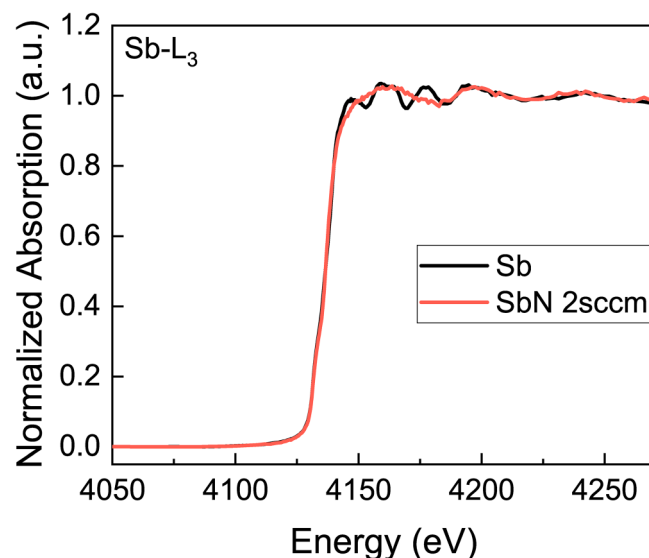


FIG. 7. XANES spectra obtained for Sb and SbN 2 sccm layers, showing the diminution of absorption features in the near-edge region for the SbN layer.

absorption features was reported in Ref. 67, related to increased disorder in the Sb structure.

The formation of Sb–N bonds is evidenced by the broad absorption band in IR spectra. Similar IR band assigned to the vibrational mode of Sb–N bonds was also observed in Ref. 68. An analogy with GeN layers can be used to identify the IR bands of SbN. The IR spectra of both Ge and Sb elemental layers feature no active modes, while the N incorporation results in a strong IR absorption in the range from  $400$  to  $800\text{ cm}^{-1}$ , composed of several contributions (identified as  $\nu_1$  and  $\nu_2$ ). The IR band of SbN is shifted toward lower wavenumbers with respect to the GeN one, since the Sb atoms are heavier (i.e., causing the changes of vibrational frequency). Considering the same coordination of Sb and N atoms, the formation of  $\text{Sb}_3\text{N}$  structural units might be suggested, similarly to  $\text{Ge}_3\text{N}$  identified in GeN layers. The two identified contributions of the main IR band ( $\nu_1$  and  $\nu_2$ ) then likely represent the Sb–N vibration of  $\text{Sb}_3\text{N}$  structural units and disorder-induced vibrations of the same units impacted by more neighboring N atoms arranged in different configurations as the N content

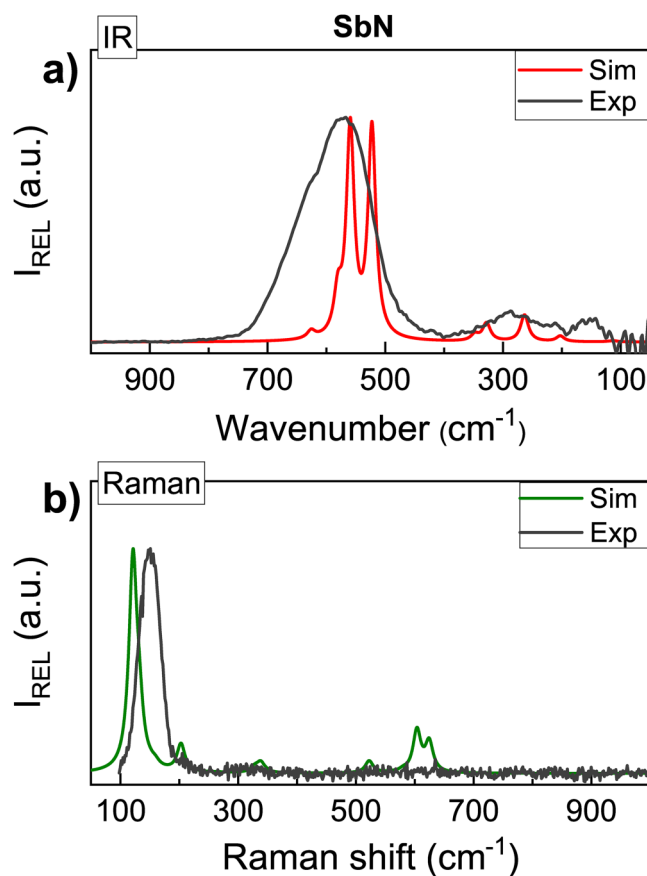
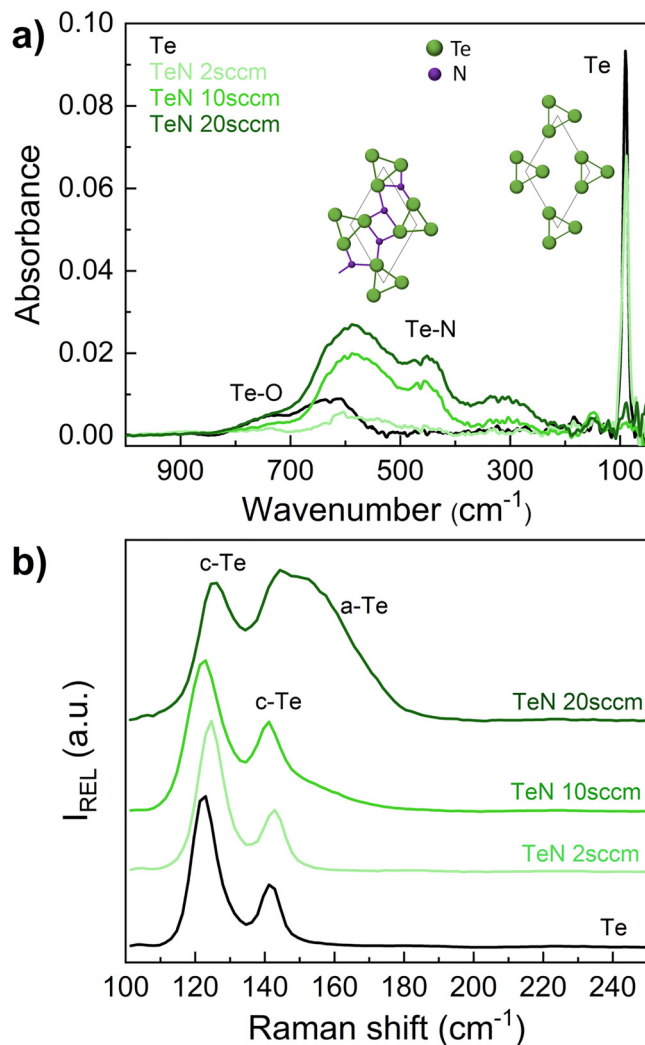


FIG. 8. Experimental (Exp) and simulated (Sim) spectra for SbN: (a) IR spectra, (b) Raman spectra. Experimental data are obtained for SbN 10 SCCM, simulated spectra results for crystalline SbN with orthorhombic structure.<sup>42</sup>



increases. The IR band  $\nu_3$  at  $300\text{ cm}^{-1}$ , also, likely results from Sb-N vibration, as its intensity increases with N content. The IR band  $\nu_4$ , on the contrary, could be likely related to Sb-Sb vibrational modes, which become IR-active due to disorder induced by N incorporation.

The experimental IR and Raman spectra were further compared with the simulated spectra of crystalline SbN with the orthorhombic structure: This comparison allows to determine the IR and Raman bands resulting from the vibration of Sb-N bonds



**FIG. 9.** IR (a) and Raman (b) spectra of Te and TeN layers. IR spectra demonstrate Te-O contribution in elemental Te layer. The broad band ( $850\text{--}250\text{ cm}^{-1}$ ) related to Te-N vibrations increases in intensity upon N incorporation, while sharp peak (at about  $90\text{ cm}^{-1}$ ) related to Te-Te vibrations is reduced. The inset sketches illustrate the N incorporation into interstitial positions between the Te chains of its crystalline structure. Raman spectra highlight two sharp peaks of crystalline Te (c-Te) and the appearance of the amorphous contribution (a-Te) upon N incorporation.

(Fig. 8). The simulated IR spectrum shows two contributions in the main band at about  $600\text{ cm}^{-1}$  and several contributions in the region around  $300\text{ cm}^{-1}$ , corresponding to the broad band observed in the experimental spectrum. Both vibrational regions can be therefore attributed to Sb-N vibration. Moreover, the contributions in both IR spectral regions correspond also in terms of intensity ratio. The simulated Raman spectrum shows a strong band at low wavenumbers and weaker bands at around  $600\text{ cm}^{-1}$ . The simulated low wavenumber band indicates a possible Sb-N contribution to the broad band assigned to a-Sb and can be likely responsible for the band shift with increasing N content. These simulated results are thus in agreement with the experimental results described above and shown in Fig. 6. A second spectral region at  $600\text{ cm}^{-1}$  assigned to the Sb-N bonds corresponds to the low intense broad band observed in the SbN 20 SCCM layer.

#### D. Te and TeN layers

The IR and Raman spectra of Te and TeN layers are shown in Fig. 9. Tellurium is highly transparent in IR, hence no contribution should be expected until far IR. Indeed, the IR spectrum of Te features a sharp peak at  $90\text{ cm}^{-1}$  corresponding to the  $A_2/E_1$  optical modes in trigonal Te (c-Te),<sup>69–71</sup> indicating that the as-deposited Te layer is crystalline. However, another broad and low intense band is observed in the range of  $550\text{--}850\text{ cm}^{-1}$  assigned to the Te-O vibrations.<sup>72,73</sup> This band indicates that the undoped Te layer is oxidized despite the deposition of the protective encapsulation layer. The oxidation of similar Te layers was observed by XPS studies.<sup>40</sup> The Raman spectrum of elemental Te layer shows two sharp peaks at  $122$  and  $142\text{ cm}^{-1}$ , assigned to the  $A_1$  and  $E_2$  modes of trigonal Te,<sup>69–71,74,75</sup> respectively. No contributions attributed to Te-O vibrations were found in the Raman spectrum.

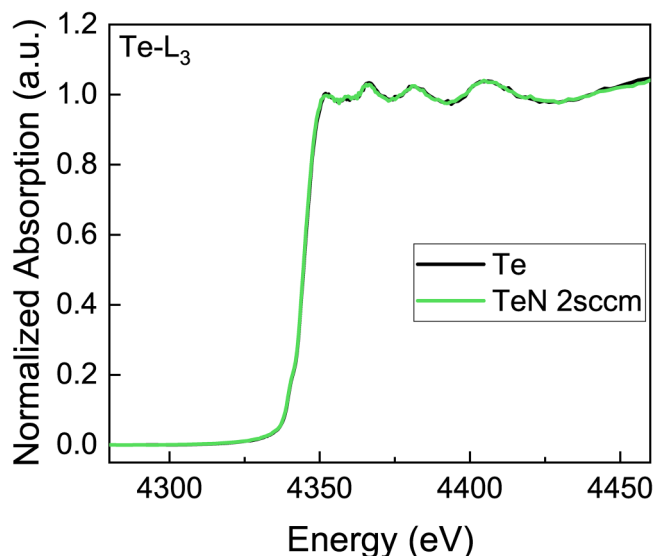


**FIG. 10.** XANES spectra obtained for Te and TeN 2 SCCM layers. The spectra do not show any significant changes upon N incorporation.

Upon N incorporation, the intensity of the Te mode at  $90\text{ cm}^{-1}$  is reduced until its complete disappearance in TeN 10 SCCM and TeN 20 SCCM layers. On the contrary, a broad band is observed in the range from  $250$  to  $850\text{ cm}^{-1}$ . Its form suggests the presence of several contributions. The IR spectra of the TeN 20 SCCM layer shows, in addition, other broad bands at higher wavenumbers (i.e.,  $4000$ – $1000\text{ cm}^{-1}$ ), corresponding to O-H, N-H, and N-O vibrations.<sup>76</sup> This range, however, is not further considered in our analysis. Raman spectra of TeN layers show a progressive broadening of the peak at  $142\text{ cm}^{-1}$ , resulting from arising additional contribution with the maximum at about  $150\text{ cm}^{-1}$ . This additional contribution has been attributed to amorphous Te (a-Te).<sup>75</sup> No other bands are observed in the Raman spectra at higher wavenumbers.

The crystalline structure of Te is known to be trigonal, composed by helical chains of Te atoms at the corners and center of a hexagonal array. The structure features the covalent bonding

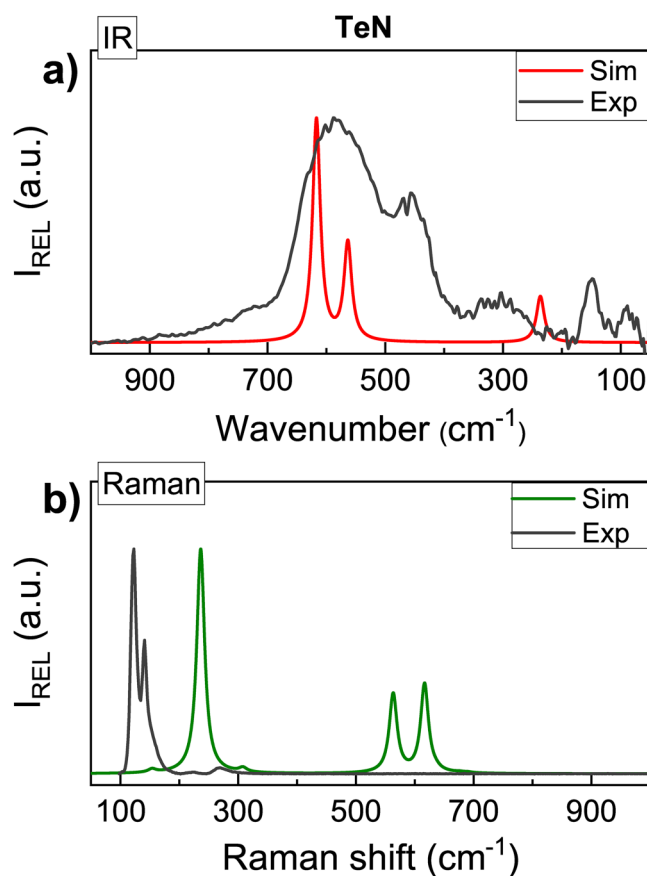


**FIG. 11.** Experimental (Exp) and simulated (Sim) spectra for TeN: (a) IR spectra, (b) Raman spectra. Experimental data are obtained for TeN10 SCCM compared to the simulated spectra of crystalline  $\text{TeN}_2$  with monoclinic structure.<sup>42</sup> The experimental Raman spectrum of TeN 10 SCCM shows only the contributions from Te-Te bonds (at  $122$  and  $142\text{ cm}^{-1}$ ).

between the atoms in the chain and secondary weaker interactions between the atoms in adjacent chains.<sup>71</sup> These secondary interactions are however stronger compared to those in S and Se structures.<sup>77</sup> This could explain lower reactivity of Te and its reduced tendency to form different compounds with regard to S and Se analogs along with the fact that Te does not build long (polymeric chains). Indeed, differently from S or Se, for which  $\text{X}_4\text{N}_4$  or  $\text{X}_2\text{N}_2$  ( $\text{X} = \text{S}, \text{Se}$ ) compounds are reported in the literature,<sup>77,78</sup> only a model structure of  $\text{Te}_3\text{N}_4$  is considered in the case of Te. Moreover, this  $\text{Te}_3\text{N}_4$  structure is considered as highly unstable and the bonding between the atoms is unknown. Te-N bonds were reported mainly in organometallic complexes, where they are, however, highly stabilized by other molecules. The low N incorporation in the structure of inorganic Te layers is also evidenced by WDXRF measurements (Fig. 1) and XANES spectra of Te and TeN layer (Fig. 10), in which N incorporation does not cause any changes in the absorption edge and adjacent absorption features.

The results of IR and Raman spectroscopy indicate that the N atoms likely occupy the interstitial positions between the covalent chains of the Te structure, having the major impact on inter-chain bonds (i.e., reduction of  $A_2$  mode at  $90\text{ cm}^{-1}$  in IR spectra), while stronger covalent intra-chain bonds are much less affected (i.e.,  $A_1$  and  $E_2$  modes at  $122$  and  $142\text{ cm}^{-1}$ , respectively, in the Raman spectra are maintained). The formation of the Te-N bonds gives rise to the broad band in the IR spectra, resulting from the induced dipole moment owing to the charge transfer between more electronegative nitrogen and less electronegative tellurium. Three band contributions can be distinguished from the performed band deconvolution (see the supplementary material), likely corresponding to three Te-N bonds between the interstitial N atom and three

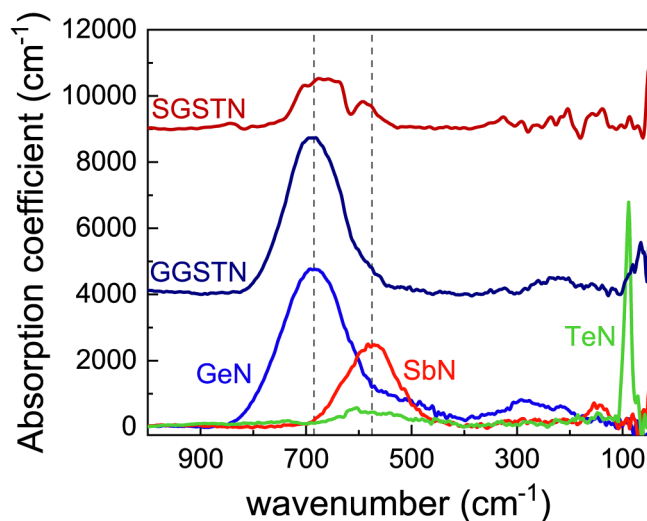


**FIG. 12.** The comparison of IR spectra of Ge, Sb, Te and Ge-rich and Sb-rich GeSbTe upon the N incorporation ( $\text{N}_2$  flow of 2 SCCM was considered for all the compared layers in our experiment). Dashed lines indicate the position of Ge-N bonds contribution in GGSTN, and Ge-N and Sb-N bonds contributions in SGSTN.

**TABLE II.** List of the position values of the IR spectra band contributions for Ge, Sb, and Te elemental and nitride systems.

		IR spectroscopy				
		$\nu_1$	$\nu_2$	$\nu_3$	$\nu_4$	$\nu_5$
Ge layer		...	...	...	...	
GeN layers		$680 \text{ cm}^{-1}$	$750 \text{ cm}^{-1}$	$280 \text{ cm}^{-1}$ (Ge-N contributions)	$390 \text{ cm}^{-1}$	
		$\nu_1$	$\nu_2$	$\nu_3$	$\nu_4$	
Sb layer		...	...	...	...	
SbN layers		$560 \text{ cm}^{-1}$	$630 \text{ cm}^{-1}$	$300 \text{ cm}^{-1}$ (Sb-N contributions)	$145 \text{ cm}^{-1}$	
		$\nu_1$	$\nu_2$	$\nu_3$	$\nu_4$	$\nu_5$
Te layer	$90 \text{ cm}^{-1}$ ( $A_2/E_1$ )	...	...	...	$635 \text{ cm}^{-1}$ (Te-O contributions)	$730 \text{ cm}^{-1}$
TeN layers	...	$570 \text{ cm}^{-1}$	$450 \text{ cm}^{-1}$ (Te-N contributions)	$315 \text{ cm}^{-1}$	$635 \text{ cm}^{-1}$ (Te-O contributions)	$730 \text{ cm}^{-1}$

closest Te atoms in adjacent Te chains. In such configurations, the N atom would maintain its lone pair, adopting its common tetrahedral configuration. Besides, the presence of N atoms with their configuration would affect the interatomic distances between the Te chains (i.e., Te atoms shift from the ideal lattice position) would lead to the modifications of the spatial arrangement of the Te chains in the structure. This effect would result in the partially disordered character of the TeN layer's structure, represented by slight broadening of the c-Te peaks and the appearance of the a-Te band in the Raman spectra.

The “*ab initio*” simulations of active vibrational modes of the crystalline TeN<sub>2</sub> monoclinic structure further support our experimental results from FTIR and Raman spectroscopy (Fig. 11). The IR spectra show a good match between the simulated and experimental results, presenting three main contributions in the band at 250-850 cm<sup>-1</sup>. On the contrary, the Raman spectrum of as-deposited TeN layer does not match with simulated TeN<sub>2</sub> structure. The vibrational modes of Te-N bonds recognized in the

simulated TeN<sub>2</sub> structure (at about 230, 560, and 630 cm<sup>-1</sup>) are not observed. This is likely due to very weak intensity of Te-N vibrations with regard to the Te-Te vibrational modes in our spectra. Indeed, the IR intensity of the broad band in the spectra reaches the maximum absorbance value of less than 0.03 for the highest N incorporation level used (Fig. 9) and the overall incorporated N content is much lower than in the case of SbN or GeN, as shown in Fig. 1.

### E. Identification of nitrogen bonding in N-doped GeSbTe alloys

Based on results presented in the previous sections, we further investigate the N bonding in more complex chalcogenide alloys. We studied two different material families recently considered for their interest for phase-change memory device integration: Ge-rich and Sb-rich GeSbTe alloys.<sup>18,22</sup> Ge-rich and Sb-rich GeSbTe layers (GGSTN and SGSTN) with low nitrogen content (<10 at. %) were

**TABLE III.** List of the position values of the Raman spectra band contributions for Ge, Sb, and Te elemental and nitride systems.

		Raman spectroscopy			
Ge layer	$100\text{--}300 \text{ cm}^{-1}$ (a-Ge modes)	...	...	...	...
GeN layers	$100\text{--}300 \text{ cm}^{-1}$ (a-Ge modes)	$600\text{--}800 \text{ cm}^{-1}$ (Ge-N contributions)	...	...	...
Sb layer	$115 \text{ cm}^{-1}$ ( $E_g$ )	$150 \text{ cm}^{-1}$ ( $A_{1g}$ )	$270 \text{ cm}^{-1}$ (second order scattering)	...	...
SbN layers	$120 \text{ cm}^{-1}$ ( $E_g$ )	$130 \text{ cm}^{-1}$ (a-Sb contribution)	$150 \text{ cm}^{-1}$ ( $A_{1g}$ )	$170 \text{ cm}^{-1}$ (SbN contribution)	...
Te layer	$122 \text{ cm}^{-1}$ ( $A_1$ )	$142 \text{ cm}^{-1}$ ( $E_2$ )	...	...	...
TeN layers	$122 \text{ cm}^{-1}$ ( $A_1$ )	$142 \text{ cm}^{-1}$ ( $E_2$ )	$150 \text{ cm}^{-1}$ (a-Te contribution)	...	...

deposited by co-sputtering of  $\text{Ge}_2\text{Sb}_2\text{Te}_5$  and Ge or Sb targets, respectively, under the same conditions as described in the experimental part, using the  $\text{N}_2$  flow of 2 SCCM. Based on our results on GeN, SbN, and TeN layers, FTIR spectroscopy is the most suitable technique for the analysis of N bonding in these alloys.

The IR spectra of Ge, Sb, Te, and GeSbTe alloys upon the N incorporation ( $\text{N}_2$  flow of 2 SCCM for all the compared layers) are shown in Fig. 12. The direct comparison of the spectra highlights the significant intensity difference and position shift of the bands assigned to the Ge-N, Sb-N, and Te-N bonds of the related elemental nitride layers. For the GGSTN, the best match is found with GeN alloy, in terms of position and shape of the observed features, thus demonstrating strong preference of the Ge-N bond formation in GGSTN alloys. The IR spectrum of SGSTN features two contributions correlated with GeN and SbN, hence indicating the formation of both Ge-N and Sb-N bonds in the system. Despite the high Sb content in SGSTN, the intensity ratio between the contributions highlights the preferential formation of Ge-N bonds over Sb-N bonds in the system.

The IR and Raman band contribution positions for all three elemental (Ge, Sb, and Te) and nitride (GeN, SbN, and TeN) systems are summarized in Tables II and III. Detailed analysis of the spectra and their deconvolutions are shown in the [supplementary material](#).

#### IV. CONCLUSIONS

This work presents the structural investigation of Ge, Sb, and Te layers upon nitrogen incorporation. By varying the  $\text{N}_2$  flow during the deposition, we observe the difference in N content in the alloys and we identify the main absorption features appearing in IR and Raman spectra. Ge layers feature the highest N incorporation, leading to the formation of Ge-N bonds in the system. The Ge-N bonds were identified owing to the IR-active vibrational modes of  $\text{Ge}_3\text{N}$  units. Sb and N present a similar bonding arrangement due to their analogous valence and coordination, which facilitates the N incorporation into the Sb structure. It leads to the Sb atom substitution, resulting in highly disordered (amorphous) structure. We suggest that the observed IR bands result from the vibration of Sb-N structural unit, similar to those identified in GeN layers. The Te layers showed to be the least prone to N incorporation, as evidenced by WDXRF measurements and the intensity of IR absorption features. The incorporated N atoms likely occupy the interstitial positions in Te crystalline structure, breaking the weak van der Waals bonds between the Te chains. It leads to a disorder induced from the lack of long-range order and the formation of Te-N bonds in the Te structure. The comparison of elemental nitride layers with off-stoichiometric Ge-rich and Sb-rich GeSbTe alloys upon nitrogen incorporation allows to identify the formation of Ge-N bonds in Ge-rich alloy and the formation of Ge-N along with Sb-N bonds in Sb-rich alloy. However, the strong preference of Ge-N bond formation was confirmed in both these off-stoichiometric ternary systems.

This study provides the analysis of the IR and Raman spectra of GeN, SbN, and TeN binary systems and the active vibrational modes resulting from N bonding, as identified with the help of “*ab initio*” simulations. These studies give the base of the nitrides

and N-doped alloys spectral analysis, which can be further completed by profound spectroscopic calculations and structure modelizations. Nevertheless, the presented results already provide the comprehensive analysis of the effects of nitrogen incorporation on the structure of Ge, Sb, and Te elemental compounds and enhance the understanding of the N doping effects on the structure of chalcogenide materials used in phase-change memory device applications.

#### SUPPLEMENTARY MATERIAL

See the [supplementary material](#) for the IR and Raman spectra deconvolution along with the parameters of band contributions of the presented GeN, SbN, and TeN systems.

#### ACKNOWLEDGMENTS

We acknowledge that part of this work has been published in L. Prazakova's PhD thesis called: Advanced Characterization for the Development of the Innovative Non-Volatile Memories.<sup>79</sup> This work was performed with the help of the NanoCharacterization Platform of Minatec with the financial support of the “Recherche Technologique de Base” program. It has been also partially funded by European commission, French State and Auvergne-Rhône Alpes region through ECSEL-IA No. 101007321 project StorAlge and French Nano2022 program. J. Li acknowledges allocation of computational resource from GENCI-IDRIS (Grant No. 2020-A0090912036). Beamtime at Elettra Sincrotrone Trieste was provided under Proposal Nos. 20175469 and 20175528, and the beamline staff (Giuliana Aquilanti and Ilaria Carlomagno) is acknowledged for their technical assistance.

#### AUTHOR DECLARATIONS

##### Conflict of Interest

The authors have no conflicts to disclose.

##### Author Contributions

**L. Prazakova:** Conceptualization (equal); Data curation (equal); Formal analysis (equal); Investigation (equal); Methodology (equal); Writing – original draft (equal); Writing – review & editing (equal). **E. Nolot:** Project administration (equal); Resources (equal); Supervision (equal); Validation (equal); Writing – review & editing (equal). **E. Martinez:** Conceptualization (equal); Methodology (equal); Project administration (equal); Supervision (equal); Validation (equal); Writing – review & editing (equal). **D. Rouchon:** Data curation (equal); Formal analysis (equal); Methodology (equal); Writing – review & editing (equal). **N. Rochat:** Data curation (equal); Formal analysis (equal); Methodology (equal); Writing – review & editing (equal). **C. Sabbione:** Conceptualization (equal); Methodology (equal); Writing – review & editing (equal). **J. Li:** Data curation (equal); Formal analysis (equal); Methodology (equal); Writing – review & editing (equal). **D. Eichert:** Data curation (equal); Formal analysis (equal); Methodology (equal); Writing – review & editing (equal). **G. Pepponi:** Formal analysis (equal); Methodology (equal); Writing – review & editing (equal). **M. Bernard:** Conceptualization

(equal); Methodology (equal). **G. Navarro:** Conceptualization (equal); Formal analysis (equal); Methodology (equal); Supervision (equal); Writing – review & editing (equal).

## DATA AVAILABILITY

The data that support the findings of this study are available from the corresponding authors upon reasonable request.

## REFERENCES

- <sup>1</sup>A. Cobelo-García, M. Filella, P. Croot, C. Frazzoli, G. Du Laing, N. Ospina-Alvarez, S. Rauch, P. Salaun, J. Schäfer, and S. Zimmermann, *Environ. Sci. Pollut. Res.* **22**, 15188 (2015).
- <sup>2</sup>P. Nuss and G. A. Blengini, *Sci. Total Environ.* **613–614**, 569 (2018).
- <sup>3</sup>S. Das, K. R. Khiangte, R. S. Fandan, J. S. Rathore, R. S. Pokharia, S. Mahapatra, and A. Laha, *Curr. Appl. Phys.* **17**, 327 (2017).
- <sup>4</sup>Y. Kamata, *Mater. Today* **11**, 30 (2008).
- <sup>5</sup>J. Liu, R. Camacho-Aguilera, J. T. Besette, X. Sun, X. Wang, Y. Cai, L. C. Kimerling, and J. Michel, *Thin Solid Films* **520**, 3354 (2012).
- <sup>6</sup>Y. Wang, Z. Ren, M. Thway, K. Lee, S. F. Yoon, I. M. Peters, T. Buonassisi, E. A. Fitzgerald, C. S. Tan, and K. H. Lee, *Sol. Energy Mater. Sol. Cells* **172**, 140 (2017).
- <sup>7</sup>X. Yu, J. Kang, R. Zhang, M. Takenaka, and S. Takagi, *Solid-State Electron.* **115**, 120 (2016).
- <sup>8</sup>B. Fang, Z. Zeng, X. Yan, and Z. Hu, *J. Mater. Sci.: Mater. Electron.* **24**, 1105 (2013).
- <sup>9</sup>K. A. Kokh, V. V. Atuchin, T. A. Gavrilo, N. V. Kuratieva, N. V. Pervukhina, and N. V. Surovtsev, *Solid State Commun.* **177**, 16 (2014).
- <sup>10</sup>J. E. Boschker, R. Wang, and R. Calarco, *CrystEngComm* **19**, 5324 (2017).
- <sup>11</sup>S. R. Ovshinsky, *Phys. Rev. Lett.* **21**, 1450 (1968).
- <sup>12</sup>N. Yamada, E. Ohno, K. Nishiuchi, N. Akahira, and M. Takao, *J. Appl. Phys.* **69**, 2849 (1991).
- <sup>13</sup>D. Ielmini and A. L. Lacaita, *Mater. Today* **14**, 600 (2011).
- <sup>14</sup>S. Raoux, W. Welnic, and D. Ielmini, *Chem. Rev.* **110**, 240 (2010).
- <sup>15</sup>G. Navarro, G. Bourgeois, J. Kluge, A. L. Serra, A. Verdy, J. Garrione, M.-C. Cyrille, N. Bernier, A. Jannaud, C. Sabbione, M. Bernard, E. Nolot, F. Fillot, P. Noe, L. Fellouh, G. Rodriguez, V. Beugin, O. Cueto, N. Castellani, J. Coignus, V. Delaye, C. Socquet-Clerc, T. Magis, C. Boixaderas, S. Barnola, and E. Nowak, in *2018 IEEE International Memory Workshop (IMW)*, Kyoto (IEEE, 2018), pp. 1–4.
- <sup>16</sup>V. Sousa, G. Navarro, N. Castellani, M. Coue, O. Cueto, C. Sabbione, P. Noe, L. Perniola, S. Blonkowski, P. Zuliani, and R. Annunziata, in *2015 Symposium on VLSI Technology* (IEEE, 2015), pp. T98–T99.
- <sup>17</sup>F. Disegni, R. Annunziata, A. Molgora, G. Campardo, P. Cappelletti, P. Zuliani, P. Ferreira, A. Ventre, G. Castagna, A. Cathelin, A. Gandolfo, F. Goller, S. Malhi, D. Manfre, A. Maurelli, C. Torti, F. Arnaud, M. Carfi, M. Perroni, M. Caruso, S. Pezzini, G. Piazza, O. Weber, and M. Peri, in *2019 Symposium on VLSI Circuits*, Kyoto (IEEE, 2019), pp. C204–C205.
- <sup>18</sup>F. Arnaud, P. Zuliani, J. P. Reynard, A. Gandolfo, F. Disegni, P. Mattavelli, E. Gomiero, G. Samanni, C. Jahan, R. Berthelon, O. Weber, E. Richard, V. Barral, A. Villaret, S. Kohler, J. C. Grenier, R. Ranica, C. Gallon, A. Souhate, D. Ristoiu, L. Favennec, V. Caubet, S. Delmedico, N. Cherault, R. Beneyton, S. Chouteau, P. O. Sassoulas, A. Vernhet, Y. L. Fric, F. Domengie, L. Scotti, D. Pacelli, J. L. Ogier, F. Boucard, S. Lagrasta, D. Benoit, L. Clement, P. Boivin, P. Ferreira, R. Annunziata, and P. Cappelletti, in *2018 IEEE International Electron Devices Meeting (IEDM)*, San Francisco, CA (IEEE, 2018), pp. 18.4.1–18.4.4.
- <sup>19</sup>S. Raoux, H.-Y. Cheng, J. Sandrini, J. Li, and J. Jordan-Sweet, in *2011 11th Annual Non-Volatile Memory Technology Symposium Proceeding*, Shanghai (IEEE, 2011), pp. 1–5.
- <sup>20</sup>P. Zuliani, E. Varesi, E. Palumbo, M. Borghi, I. Tortorelli, D. Erbetta, G. D. Libera, N. Pessina, A. Gandolfo, C. Prelini, L. Ravazzi, and R. Annunziata, *IEEE Trans. Electron Devices* **60**, 4020 (2013).
- <sup>21</sup>P. Zuliani, E. Palumbo, M. Borghi, G. Dalla Libera, and R. Annunziata, *Solid-State Electron.* **111**, 27 (2015).
- <sup>22</sup>G. Navarro, C. Sabbione, M. Bernard, G. Bourgeois, J. Sandrini, N. Castellani, O. Cueto, J. Garrione, M. C. Cyrille, M. Frei, L. Nistor, N. Bernier, F. Fillot, E. Nolot, C. Socquet-Clerc, T. Magis, F. Laulagnet, M. Pakala, and E. Nowak, in *2019 IEEE 11th International Memory Workshop (IMW)*, Monterey, CA (IEEE, 2019), pp. 1–4.
- <sup>23</sup>X. Li, H. Chen, C. Xie, D. Cai, S. Song, Y. Chen, Y. Lei, M. Zhu, and Z. T. Song, *Phys. Status Solidi RRL* **13**, 1800558 (2019).
- <sup>24</sup>H. Y. Cheng, J. Y. Wu, R. Cheek, S. Raoux, M. BrightSky, D. Garbin, S. Kim, T. H. Hsu, Y. Zhu, E. K. Lai, E. Joseph, A. Schrott, S. C. Lai, A. Ray, H. L. Lung, and C. Lam, in *2012 International Electron Devices Meeting*, San Francisco, CA (IEEE, 2012), pp. 31.1.1–31.1.4.
- <sup>25</sup>H. Y. Cheng, M. BrightSky, S. Raoux, C. F. Chen, P. Y. Du, J. Y. Wu, Y. Y. Lin, T. H. Hsu, Y. Zhu, S. Kim, C. M. Lin, A. Ray, H. L. Lung, and C. Lam, in *2013 IEEE International Electron Devices Meeting*, Washington, DC (IEEE, 2013), pp. 30.6.1–30.6.4.
- <sup>26</sup>T. H. Jeong, M. R. Kim, H. Seo, J. W. Park, and C. Yeon, *Jpn. J. Appl. Phys.* **39**, 2775 (2000).
- <sup>27</sup>S. Kozyukhin, V. Kudoyarova, H. P. Nguyen, A. Smirnov, and V. Lebedev, *Phys. Status Solidi C* **8**, 2688 (2011).
- <sup>28</sup>R. Sinha-Roy, A. Louiset, M. Benoit, and L. Calmels, *Phys. Rev. B* **99**, 245124 (2019).
- <sup>29</sup>R. Golovchak, Y. G. Choi, S. Kozyukhin, Y. Chigirinsky, A. Kovalskiy, P. Xiong-Skiba, J. Trimble, R. Pafchek, and H. Jain, *Appl. Surf. Sci.* **332**, 533 (2015).
- <sup>30</sup>R. Kojima, S. Okabayashi, T. Kashihiro, K. Horai, T. Matsunaga, E. Ohno, N. Yamada, and T. Ohta, *Jpn. J. Appl. Phys.* **37**, 2098 (1998).
- <sup>31</sup>G. Navarro, V. Sousa, P. Noe, N. Castellani, M. Coue, J. Kluge, A. Kiouseloglou, C. Sabbione, A. Persico, A. Roule, O. Cueto, S. Blonkowski, F. Fillot, N. Bernier, R. Annunziata, M. Borghi, E. Palumbo, P. Zuliani, and L. Perniola, in *2016 IEEE 8th International Memory Workshop (IMW)*, Paris, France (IEEE, 2016), pp. 1–4.
- <sup>32</sup>D. Dimitrov and H.-P. D. Shieh, *Mater. Sci. Eng. B* **107**, 107 (2004).
- <sup>33</sup>L. Cheng, L. Wu, Z. Song, F. Rao, C. Peng, D. Yao, B. Liu, and L. Xu, *J. Appl. Phys.* **113**, 044514 (2013).
- <sup>34</sup>W. C. Johnson, *J. Am. Chem. Soc.* **52**, 5160 (1930).
- <sup>35</sup>P. V. Pavlov, E. I. Zorin, D. I. Tetelbaum, and A. F. Khokhlov, *Phys. Stat. Sol. A* **35**, 11 (1976).
- <sup>36</sup>M. I. Baraton, R. Marchand, and P. Quintard, *J. Mol. Struct.* **143**, 9 (1986).
- <sup>37</sup>F. Boscherini, A. Filippini, S. Pascarelli, F. Evangelisti, S. Mobilio, F. C. Marques, and I. Chambouleyron, *Phys. Rev. B* **39**, 8364 (1989).
- <sup>38</sup>S. S. Makler, G. Martins da Rocha, and E. V. Anda, *Phys. Rev. B* **41**, 5857 (1990).
- <sup>39</sup>I. Chambouleyron and A. R. Zanatta, *J. Appl. Phys.* **84**, 1 (1998).
- <sup>40</sup>E. Nolot, C. Sabbione, W. Pessoa, L. Prazakova, and G. Navarro, *Appl. Surf. Sci.* **536**, 147703 (2021).
- <sup>41</sup>W. Sun, C. J. Bartel, E. Arca, S. R. Bauers, B. Matthews, B. Orvañanos, B.-R. Chen, M. F. Toney, L. T. Schelhas, W. Tumas, J. Tate, A. Zakutayev, S. Lany, A. M. Holder, and G. Ceder, *Nat. Mater.* **18**, 732 (2019).
- <sup>42</sup>See <https://materialsproject.org/> for “Materials Data on Ge<sub>3</sub>N<sub>4</sub> (mp-13852), SbN (mp-1271276) and TeN<sub>2</sub> (mvc-13772) structures by Materials Project” (2020).
- <sup>43</sup>M. Bjorgvinsson and H. W. Roesky, *Polyhedron* **10**, 2353 (1991).
- <sup>44</sup>T. Chivers, *J. Chem. Soc., Dalton Trans.* **1996**, 1185 (1996).
- <sup>45</sup>L. Lian, Y. Liu, D. Li, and S. Wei, *RSC Adv.* **10**, 2448 (2020).
- <sup>46</sup>Y. Hu, X. Zhu, H. Zou, J. Zhang, L. Yuan, J. Xue, Y. Sui, W. Wu, S. Song, and Z. Song, *Appl. Phys. Lett.* **108**, 223103 (2016).
- <sup>47</sup>C. Jaynes, E. Nolot, C. Costa, C. Sabbione, W. Pessoa, F. Pierre, A. Roule, G. Navarro, and M. Mantler, *J. Anal. At. Spectrom.* **35**, 701 (2020).



- <sup>48</sup>A. L. Ankudinov, B. Ravel, J. J. Rehr, and S. D. Conradson, *Phys. Rev. B* **58**, 7565 (1998).
- <sup>49</sup>G. Kresse and J. Furthmüller, *Phys. Rev. B* **54**, 11169 (1996).
- <sup>50</sup>G. Kresse and D. Joubert, *Phys. Rev. B* **59**, 1758 (1999).
- <sup>51</sup>J. M. Skelton, L. A. Burton, A. J. Jackson, F. Oba, S. C. Parker, and A. Walsh, *Phys. Chem. Chem. Phys.* **19**, 12452 (2017).
- <sup>52</sup>J. P. Perdew, K. Burke, and M. Ernzerhof, *Phys. Rev. Lett.* **77**, 3865 (1996).
- <sup>53</sup>F. C. Marques, I. Chambouleyron, and F. Evangelisti, *J. Non-Cryst. Solids* **114**, 561 (1989).
- <sup>54</sup>C. Guanghua and Z. Fangqing, *Thin Solid Films* **185**, 231 (1990).
- <sup>55</sup>A. R. Zanatta and I. Chambouleyron, *Phys. Rev. B* **48**, 4560 (1993).
- <sup>56</sup>J. S. Lannin, N. Maley, and S. T. Kshirsagar, *Solid State Commun.* **53**, 939 (1985).
- <sup>57</sup>P. Kazimierski, J. Tyczkowski, M. Kozanecki, Y. Hatanaka, and T. Aoki, *Chem. Mater.* **14**, 4694 (2002).
- <sup>58</sup>P. A. Temple and C. E. Hathaway, *Phys. Rev. B* **7**, 3685 (1973).
- <sup>59</sup>A. Zwick and R. Carles, *Phys. Rev. B* **48**, 6024 (1993).
- <sup>60</sup>Y. Kim, M. H. Jang, K. Jeong, M.-H. Cho, K. H. Do, D.-H. Ko, H. C. Sohn, and M. G. Kim, *Appl. Phys. Lett.* **92**, 061910 (2008).
- <sup>61</sup>E. Soignard and P. F. McMillan, *Chem. Mater.* **16**, 3533 (2004).
- <sup>62</sup>J. B. Renucci, W. Richter, M. Cardona, and E. SchÖsther, *Phys. Status Solidi B* **60**, 299 (1973).
- <sup>63</sup>J. S. Lannin, J. M. Calleja, and M. Cardona, *Phys. Rev. B* **12**, 585 (1975).
- <sup>64</sup>J. S. Lannin, *Phys. Rev. B* **15**, 3863 (1977).
- <sup>65</sup>M. Mayo, E. Yahel, Y. Greenberg, and G. Makov, *J. Phys.: Condens. Matter* **25**, 505102 (2013).
- <sup>66</sup>J. Buckeridge, D. O. Scanlon, T. D. Veal, M. J. Ashwin, A. Walsh, and C. R. A. Catlow, *Phys. Rev. B* **89**, 014107 (2014).
- <sup>67</sup>J. M. Charnock, K. E. R. England, C. M. B. Henderson, J. F. W. Mosselmanns, and R. A. D. Patrick, *J. Phys. IV France* **7**, C2 (1997).
- <sup>68</sup>T. Shiraishi, Y. Arai, and S. Yamazaki, *J. Non-Cryst. Solids* **77-78**, 1313 (1985).
- <sup>69</sup>G. Lucovsky, R. C. Keezer, and E. Burstein, *Solid State Commun.* **5**, 439 (1967).
- <sup>70</sup>B. H. Torrie, *Solid State Commun.* **8**, 1899 (1970).
- <sup>71</sup>G. Lucovsky, *Phys. Stat. Sol. B* **49**, 633 (1972).
- <sup>72</sup>Y. Dimitriev, V. Dimitrov, and M. Arnaudov, *J. Mater. Sci.* **18**, 1353 (1983).
- <sup>73</sup>R. A. El-Mallawany, *Infrared Phys.* **29**, 781 (1989).
- <sup>74</sup>A. S. Pine and G. Dresselhaus, *Phys. Rev. B* **4**, 356 (1971).
- <sup>75</sup>M. H. Brodsky, R. J. Gambino, J. E. Smith, and Y. Yacoby, *Phys. Stat. Sol. B* **52**, 609 (1972).
- <sup>76</sup>P. Larkin, *Infrared and Raman Spectroscopy* (Elsevier, 2011).
- <sup>77</sup>T. Chivers and R. S. Laitinen, *Chem. Soc. Rev.* **44**, 1725 (2015).
- <sup>78</sup>T. Chivers and R. S. Laitinen, *Dalton Trans.* **49**, 6532 (2020).
- <sup>79</sup>L. Prazakova, *Advanced Characterization for the Development of the Innovative Non-Volatile Memories* (Université Grenoble-Alpes, 2022).